Investigation of Trapped Vorticity Concentrations Effected by Hybrid Actuation in an Offset Diffuser

Travis J. Burrows[*], Zicheng Gong[*], Bojan Vukasinovic[†] and Ari Glezer[‡]
Woodruff School of Mechanical Engineering,
Georgia Institute of Technology, Atlanta, GA 30332-0405

Trapped vorticity concentration engendered by deliberate modification of the internal surface of an offset diffuser is coupled with a spanwise array of surface-integrated fluidic-oscillating jets for hybrid flow control of the secondary flow that gives rise to flow distortions. The trapped vorticity mimics the effects of local separation within aggressive diffusers and is used as a testbed for investigations of the effectiveness of such hybrid flow control for alleviation the flow distortions at the engine inlet (AIP). The local and global characteristics of the diffuser flow in the absence and presence of the actuation are investigated at Mach numbers up to $M = 0.7$, using a forty-probe AIP total pressure rake, surface oil-flow visualization, hot-wire anemometry, and particle image velocimetry. The present investigations demonstrate that the actuation affects the strength and scale of the trapped vorticity and its interaction with the cross flow, and consequently alters the flow evolution within the diffuser and leads to significant suppression of pressure distortion at the AIP (by about 80%). These findings indicate that hybrid actuation based on trapped vorticity concentrations can be utilized for mitigation of flow distortion in diffuser flows by strong coupling to the natural formation of vorticity concentrations due to the local flow separation.

Nomenclature

AIP	aerodynamic interface plane	p_t	total pressure
C_q	jet mass flow rate coefficient	q	planar velocity magnitude
D	diffuser AIP diameter	U	streamwise velocity
$DPCP_{avg}$	average SAE circumferential distortion descriptor	$U+$	U/u_τ
f	frequency	u_τ	friction velocity
H	diffuser inlet height	w	jet orifice width
L	diffuser length	$y+$	wall coordinate
M	Mach number	ρ	air density
psd	power spectral density	ν	kinematic viscosity

I. Technical Background

Next-generation carrier-based supersonic aircraft will use embedded engines to attain both aerodynamic efficiency and small spot factor with extremely compact inlet system that will have to be offset, potentially in multiple planes to enable efficient inlet/airframe integration schemes. The realization of these compact, offset inlet systems poses significant technical challenges in terms of flow management in the two primary system elements, namely the supersonic inlet aperture and the compact, subsonic offset diffuser. The flow within the subsonic offset diffuser is dominated by the evolution of three-dimensional, secondary structures and by possible internal flow separation which can be affected by and even become coupled to shock-induced flow unsteadiness at the inlet aperture. Overall, these complex internal flow interactions result in significant total pressure losses and flow distortion at the engine face that could be mitigated by the development and implementation of new, active flow-control (AFC) technologies upstream of the inlet aperture and within the offset diffuser. The primary focus of the present study is

[*] Graduate Research Assistant, AIAA Member.
[†] Research Engineer, AIAA Member.
[‡] Professor, Associate Fellow AIAA.

the application of flow control technologies to mitigate the formation of three-dimensional vortical structures and flow separation within aggressive offset diffusers and thereby minimize losses and flow distortions leading into an engine.

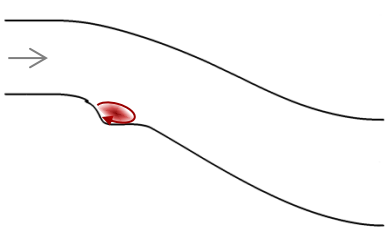

Figure 1. *Trapped vorticity in an offset diffuser.*

The flow control approach that is proposed in this work is aimed at the existing local flow separation bubble within the diffuser, as illustrated in Figure 1. The objective is to utilize an active control of the trapped vorticity within the separation bubble, which in turn affects the separated and secondary flows within the diffuser and thereby mitigates adverse effects of the flow losses and distortion. The proposed flow control approach effects fluidic modification of the "apparent" aerodynamic shape of the diffuser's flow boundary about the separation bubble, with the objective of altering or prescribing the streamwise pressure gradient to alter the evolution of the internal boundary layer and thereby suppress or mitigate local separation and the evolution of the resulting streamwise vortical structures downstream from the flow reattachment.

The physically robust, passive flow control techniques that have been successfully applied to inlet systems to improve AIP (aerodynamic interface plane) total-pressure recovery and distortion[1,2,3,4] inherently lack real-time adjustability of the actuation and also result in pressure losses at or near the flow boundary. In a study by Anderson and Gibb[5] a row of vane type vortex generators in an S-duct diffuser was found to reduce distortion and increase pressure recovery at the exit plane of the inlet. The reduction of the distortion effects induced by the ingestion of a thick boundary layer by using vane arrays was investigated by Anabtawi et al.[6]. More recently, Anderson et al.[7] have demonstrated in a numerical study the control effectiveness of passive, vane type vortex generators having a characteristic cross stream scale that was selected to be a fraction of the boundary layer height to reduce losses. In a later numerical investigation, Anderson et al.[8] showed that small-scale ("micro") vanes can be used to reduce pressure distortion at the exit plane of compact offset diffusers. Experimental work by Jirásek[4] on complex, D-throat, heavily offset inlets further corroborated the efficacy of sub-boundary layer vane actuators. Tournier and Paduano[9] used two rows of vane type vortex generators to produce arrays of single-sense streamwise vortices in an offset diffuser at $M = 0.6$ with deliberately-imposed inlet distortions, and reported marked improvements in pressure distortion at the exit plane. Owens et al.[3] used a single row of vortex generators in an S-duct diffuser operating in a free stream at $M = 0.85$ resulting in a reduction of the circumferential distortion levels at the engine face. Sub-boundary layer passive flow control devices (micro-ramps) for controlling shock wave boundary layer interactions were investigated via experimentally-validated numerical computations in a supersonic inlet[10]. These authors reported that these vortex generators significantly reduced the interactions and their unsteady effects on the outer flow field. Micro-ramps similar to those used by Anderson et al.[10] were also investigated experimentally[11] and showed performance gains in terms of reduced shock-induced separation.

Active flow control approaches that rely on distributions of normal and skewed jets emanating from the inner surfaces of the inlet duct can lead to significant improvement in the performance of offset diffusers with potential for rapid actuation and little drag penalty in the absence of actuation. AFC affords optimization and in-flight performance control both in the absence[12,13,14] and presence[15,16] of flow separation. Amitay et al.[17] demonstrated active flow control of localized separation in internal flows in a two-dimensional S-duct using a synthetic jet control. Anderson et al.[14] preformed a DOE analysis to optimize the use of skewed jets with significant improvements in pressure recovery and engine face distortion. Scribben et al.[13] used vortex generator jets in a complex offset diffuser and showed drastic improvements in distortion levels and a small reduction in drag. In similar experiments, Owens et al.[3] used various arrays of vortex generator jets in a S-duct diffuser at $M = 0.85$ to gain insight into optimal design. More recently, Gissen et al.[18] developed different configurations of synthetic jet arrays that generated fluidic counterparts to passive sub-boundary layer control devices in high subsonic flow in a 2D equivalent of an offset diffuser.

More recently, a hybrid control approach, which incorporates the advantages of both passive and active control has been shown to be effective for reduction of parasitic drag while maintaining fail-safe attributes and satisfying the need for adjustable flow control[3,19]. Owens et al.[3] combined active and passive flow control using micro-vanes and -jets to improve the performance of an offset diffuser over a range of flow rates, especially at low velocities for which the micro-vanes were not optimized. In an effort to reduce engine bleed, Anderson et al.[19] combined the micro-ramps used in their earlier work[10] with flow injection resulting in an almost 10-fold reduction in required engine bleed. Vane type vortex generators have been extensively studied as a means for controlling separation in adverse pressure gradients[20], as well as for use in s-ducts[6,8,9] and as the passive component of hybrid flow control systems[3,21]. Nonlinear superposition

of active and passive devices to create a fail-safe adjustable hybrid flow control device can be highly-effective performance enhancers for embedded propulsion systems with minimal system-level penalties in terms of weight, power consumption, robustness and maintenance.

Delot, Garnier, and Pagan[22] experimentally evaluated the effectiveness of passive flow control with vortex generators as well as active flow control with continuous and pulsed micro-jets on reducing the AIP flow distortion in a subsonic offset diffuser, and reported a reduction by 50% at $M = 0.2$ and up to 20% at $M = 0.4$. Harrison et al.[23] simulated and experimentally verified the effect of various blowing and suction flow control schemes on a thick boundary layer ingesting serpentine diffuser using swirl and circumferential flow distortion analysis. It is found that when using a circumferential blowing scheme, a 50% reduction of total pressure distortion can be realized. In addition, they also noted that a combination of blowing and suction can produce even higher reductions in distortion of 75%. Gissen et al.[24,25] used hybrid flow control in an offset diffuser and showed reductions in AIP distortion levels under both active and hybrid control. They also indicated that the governing mechanism behind active redistribution of low momentum fluid in the diffuser is in dynamics of a large-scale counter-rotating pair of vortices that are formed after a merger of the array of small-scale vortices imposed by the flow control. Gartner and Amitay[26] studied the effect of introducing a honeycomb mesh upstream of an offset rectangular duct, and showed that the use of a honeycomb mesh can improve the symmetry of the pressure distribution while minimally decreasing the pressure recovery by pushing the saddle-saddle point of flow that causes the onset of an instability responsible for the asymmetry of the flow, further downstream. Gartner and Amitay[27] experimentally tested the effect of sweeping, pulsed, and two-dimensional jet actuators on the pressure recovery of a rectangular diffuser under transonic flow conditions, and showed that the sweeping jets produced higher pressure recovery at comparable mass flow rates.

II. Experimental Setup and Diagnostics Techniques

The experiments are performed in a small, open-return, pull-down, high-speed subsonic wind tunnel (test sections speeds of up to $M \approx 0.75$). The tunnel is driven by a 150 HP blower, where the temperature of the return air is controlled using a chiller, coupled with an ultra low pressure drop heat exchanger. Instead of the tunnel test section, the offset diffuser model is installed such that it couples upstream to the tunnel inlet contraction. Diffuser geometry is shown in Figure 2, having a D-shaped throat of $H = 8.9$ cm in height, and a round, aerodynamic interface plane (AIP) with a diameter, $D = D_{AIP} = 12.7$ cm, while the offset between the throat and AIP is $1 \cdot D_{AIP}$.

Figure 3a illustrates diffuser integrated into the wind tunnel. The upstream section of the diffuser lower surface incorporates a large, removable flow control insert, spanning -0.5" < x < 5.5" that is designed to accept a variety of flow control devices. The main flow diagnostic equipment integrated into the diffuser includes a standard total pressure rake to measure the flow distortion at the AIP according to the industry standard ARP1420b[28], having a total of 40 probes in eight, equiangularly spaced rakes around the circumference of the AIP (Figure 3a inset). The rake assembly was designed such that the steady-state total pressure rakes can be interchangeable with dynamic total pressure rakes for the acquisition of dynamic distortion data. The AIP total pressure rake is supplemented with a matching ring of eight static pressure ports along the diffuser wall, at the base of each rake leg. In addition, twelve and five static pressure ports are distributed along the bottom and top side of the diffuser wall, respectively. Static and total pressures are measured using a dedicated PSI Netscanner system. Each set of pressure measurements is based on sixty four independent samples, while the mean static and total pressures are based on one hundred data sets. Consequently, uncertainty in the mean pressures is estimated to be less than 1%. Also, a derived $DPCP_{avg}$ parameter is estimated to have uncertainty of less than 2%. Calibration of the offset duct facility was performed relative to the reference static pressure port upstream from the duct inlet and the corresponding flow Mach number is based on the mean rake total pressure and the mean matching wall static pressure. In addition to the static and total pressure measurements, duct surface oil-flow visualization and localized visualization of the 'near field' across the control surface are utilized to elucidate the wall flow topology and shed a light on the local and global flow dynamics.

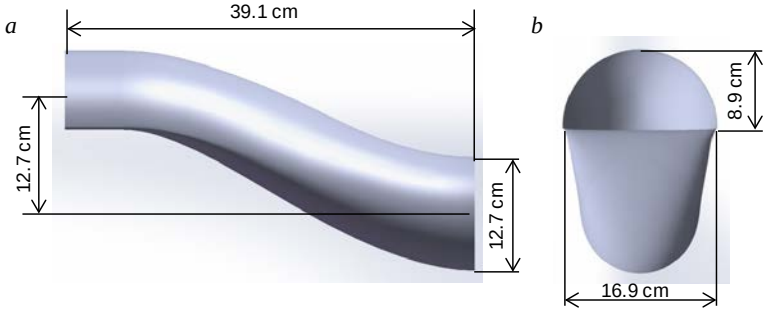

Figure 2. *Offset diffuser geometry.*

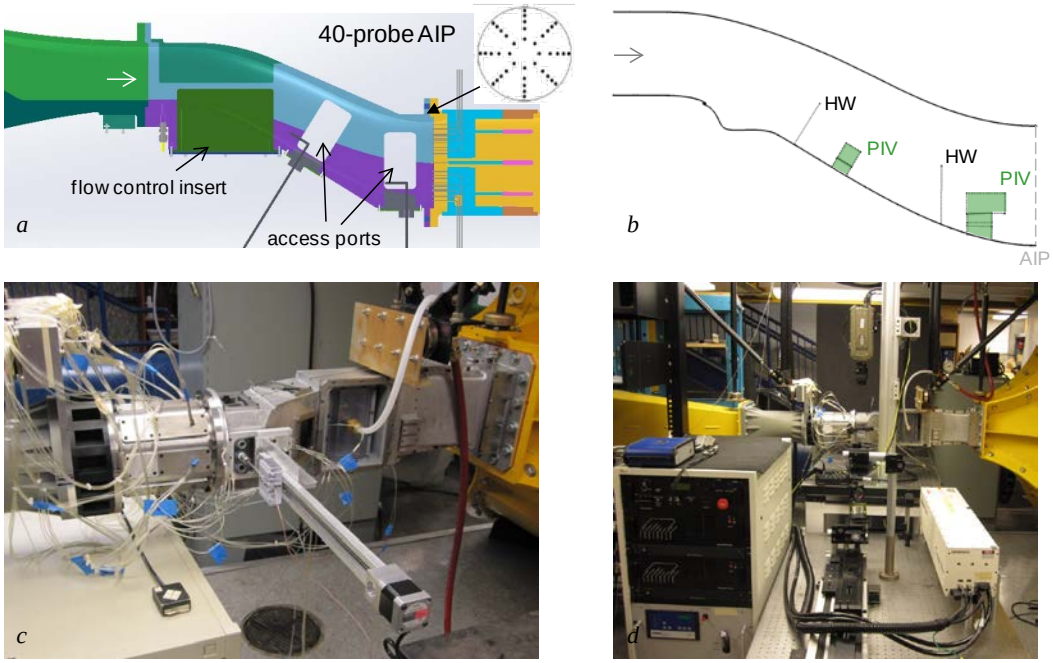

Figure 3. *A model of the offset diffuser (a) and the flow characterization domains for the hot-wire (HW) and PIV measurements (b), and experimental setups for the HW (c) and PIV (d) diagnostics.*

Diffuser flow characterization, with and without the flow control, is done by the hot-wire anemometry (HWA) and particle image velocimetry (PIV) measurements over the two measurement domains, namely downstream from the flow reattachment and upstream from the AIP, as shown in Figure 3b. Both measurement techniques utilize two pairs of access ports (Figure 3a) that are nominally blank windows. The hot-wire probe is mounted on a linear traverse with a stepper motor, which is computer-controlled and traversed away from the wall across a path shown at each of the measurement locations in Figure 3b, such that its measurements extend deep into the diffuser. As the hot wire probe responds to unit mass flow rate $\rho \cdot q$ in compressible flows (where q is an planar velocity component defined by the hot wire orientation), all measurement results are shown scaled with ρ_o and c as $\rho^* \cdot M = \rho/\rho_o \cdot (q/c)$. Besides the averaged and RMS $\rho \cdot q$ profiles, additional frequency-resolving measurements are taken at characteristic points across such profiles that give an insight into spectral energy distributions of $\rho \cdot q$ fluctuations. An image depicting the hot-wire measurements hardware at the AIP measurement location is shown in Figure 3c.

While the hot-wire anemometry enables high temporal resolution (~ 20 kHz) at individual measurement points, PIV is further utilized for additional flow diagnostics with high spatial ($\Delta \approx 300$ μm) and reduced temporal resolution (PIV sampling rate of 3 kHz) of near-wall regions downstream from the reattachment and upstream from the AIP, as shown in Figure 3b. PIV diagnostics included a design and assembly of the optical setup for the laser sheet illumination of the diffuser central plane, along with the high-speed PIV laser and the *Phantom* high-speed camera. A challenge in PIV implementation in 3-D internal geometries is in enabling the optical access from two nominally orthogonal views, one for the laser-sheet illumination, and the other one for the PIV camera imaging. This is accomplished in the current model by utilization of a pair of the access ports (Figure 3a). For this purpose, the blank windows that fit into the access ports are remanufactured such that each has a narrow receptacle that

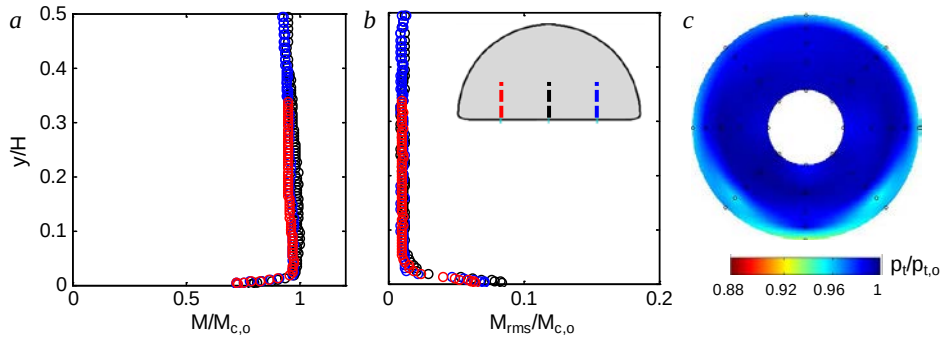

Figure 4. *Mach (a) and the Mach RMS (b) profiles of the diffuser oncoming boundary layer at three spanwise locations (see inset), and the contour plot of the corresponding total pressure (c) measured by the 40-probe AIP rake.*

seats small glass inserts. These glass inserts are then used for optical access for both the laser sheet and the camera view. Upstream PIV domain consists of the two partially overlapping views of about 18 × 18 mm, while the AIP domain has a single larger field of view away from the wall that is about 40 × 20 mm, and two smaller partially overlapping views of about 26 × 14 mm. Each PIV data set is typically taken over 1,000 image pairs and recorded at 2 kHz sampling rate, such that the spatial vector field resolution is about 0.3 mm. The PIV setup is shown in Figure 3d.

III. Hybrid Flow Control Configuration

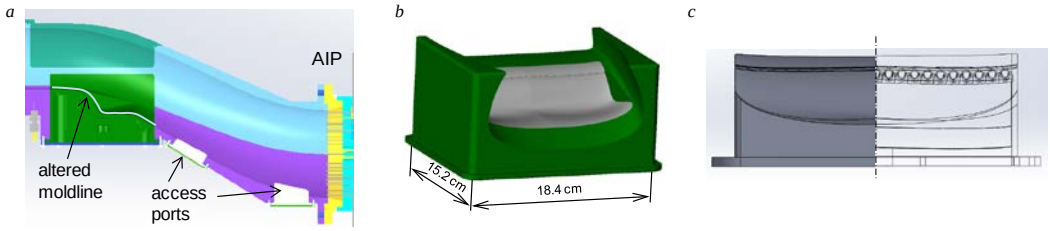

Figure 5. *Schematics of the diffuser passive geometry modification (a), integrated flow control module (b), and its array of fluidic oscillating jets (c).*

The objective of this study is to exploit trapped vorticity concentrations to affect global modification of the base flow and thereby control flow distortion at the diffuser's AIP and improve the diffuser's performance. In the absence of any hybrid modifications, diffuser flow in the geometry shown in Figure 2 has minimal distortion at the AIP, if the incoming boundary layer is thin. This is illustrated in Figure 4 where the diffuser approach flow is characterized by hot-wire measurements at an axial station of x/H = -1, where x = 0 is defined at the diffuser throat. Measurements are done at three spanwise locations, z/H = -0.5, 0, and 0.5 that are marked in inset plot of Figure 4b. The resulting profiles of the mean velocity and RMS velocity fluctuations are shown in Figure 4a and b, respectively, which indicate that the high-shear region associated with the boundary layer is confined to immediate vicinity of the wall, within about 2 mm away from the surface. Furthermore, symmetry of the profiles about the central plane (z/H = 0) indicates a rather uniform approach boundary layer away from the corners. Such a thin incoming vorticity layer evolves in a rather weak and thin secondary flow along the diffuser's path, which results in nearly negligible total pressure distortion at the AIP, as shown in Figure 4c, where the average distortion parameter $DPCP_{avg}$ is only about 0.008.

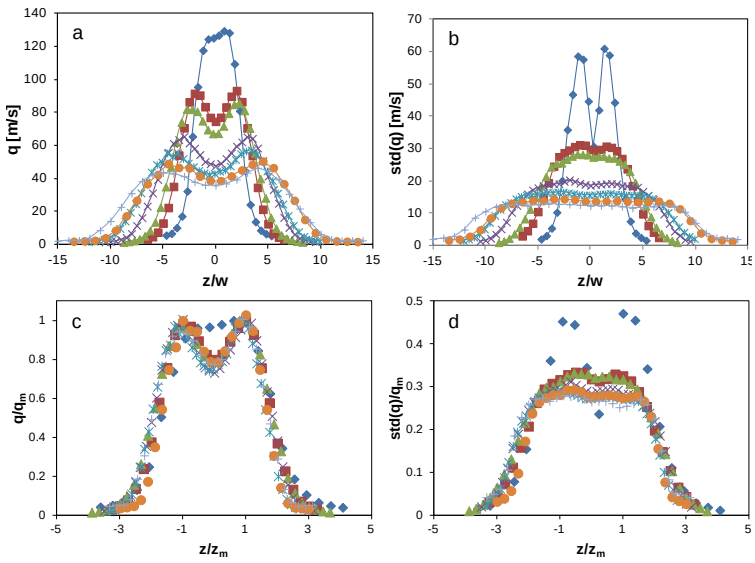

Figure 6. *Time-averaged velocity magnitude q (a, c) and its standard deviation (b, d) profiles for an isolated fluidic-oscillating jet issuing into quiescent air at downstream positions x/w = 5 (♦), 7.5 (■), 10 (▲), 12.5 (×), 15 (*), 17.5 (●).*

In order to mimic recirculating bubble due to a local flow separation in an aggressive diffuser, a passive modification of the upstream diffuser moldline is made, as schematically shown in Figure 5a, where the recessed moldline smoothly mates with both the upstream and downstream diffuser surfaces. This passive geometry modification is made within a large removable diffuser module (Figure 5b) that carries the hybrid flow control insert. The active part of this hybrid flow control approach consists of an array of fluidic oscillating jets that are distributed across a span of the module. The flow control jets are positioned immediately upstream of the origin of flow separation, which was determined by surface oil-flow visualization over a blank insert. Figure 5c illustrates the array of fluidic oscillating jets utilized in this study, shown only over half of the module span. The present configuration includes twenty one fluidic oscillating jets that are equally spaced (7

mm apart) along the span of the control insert. Each jet orifice measures 1.24 × 1.5 mm in its nominal configuration, having the operating frequency between f = 7 – 9 kHz over a range of operation. The jets aim at direct control of the strength and structure of the trapped vorticity concentration, and thereby affecting the global flow within the diffuser.

A single fluidic-oscillating jet is first tested on a bench by hot-wire anemometry (HWA). This individual jet module is held stationary, while the hot-wire probe is traversed by a computer-controlled stepper motors. Profiles of the mean in-plane velocities and their RMS fluctuations are measured at seven downstream locations at x/w = 5 – 20 relative to the jet orifice, where w is the orifice width. Families of the velocity and RMS profiles for a given flow rate through the actuator are shown in Figure 6. The dimensional profiles (Figures 6a and b) indicate that all but the closest profile exhibit a typical saddle velocity profile, where the peak locations indicate predominant jet directions in the limit states of oscillation. Both the closest RMS and velocity profiles (x/w = 5) indicate a possible transitional region prior to full jet oscillation, where the jet profile is of bell-shape type, while the RMS fluctuations are the highest about each shear layer boundary. As there is no dominant length scale in the free-evolving oscillating jet, it is to be expected that its evolution depends only on the local velocity and length scales. Hence, when the distances are scaled by the local half-width of the velocity peak z_m and profiles by the local velocity peak q_m, all but the closest, still evolving profile fall on the universal profiles shown in Figure 6c and d.

IV. Flow Control Effects

Global effectiveness of the hybrid flow control approach is first demonstrated over a range of the diffuser Mach numbers M = 0.36 – 0.7. For each of the base flows, total pressure distortion estimate $DPCP_{avg}$ is based on the 40-probe rake measurements at the AIP for the flow uncontrolled, and controlled by the fixed total flow rate through the control jets. All the base flow total pressure contours are shown in Figures 7a–e, where the same distortion pattern (i.e., reduced total pressure) is observed, only increasing in strength with M: a sharp cusped distortion is centered about the bottom-wall plane of symmetry, terminating over a thin wall layer in outward direction. It is interesting to note that such a total pressure deficit in the base has a shape that is nearly identical to that of a thick boundary layer-ingesting (BLI) offset diffuser without internal flow separation[24,25]. This similarity may imply that similar flow dynamics is responsible for the loss of momentum/total pressure within analogous regions of the flow. In the BLI offset diffuser, the AIP total pressure distortion pattern is formed by the action of an induced pair of large-scale secondary vortices that act such to redistribute incoming large momentum deficit of the boundary layer to the bottom central zone of the AIP. In the present experiments, there is no large momentum deficit carried into the diffuser, but it is rather generated over and downstream of the separation bubble. It can be argued that the "focusing" of the low momentum flow about the lower central portion of the AIP is done by a mechanism similar to the BLI diffuser. It is postulated that a similar large-scale secondary flow is primarily triggered by turning of the initial predominantly spanwise vortex lines, due to the leading central flow and the trailing corner-wall flow. This results in two large-scale counter-rotating vortical structures having a sense of vorticity such that they bring high momentum fluid from the upper side walls and push the low momentum fluid towards the central lower zone. As the flow control is applied for each of the base cases (Figures 7f–j), it induces a redistribution of low momentum fluid from the central cusped zone down and outward along the wall, thus forming a thin layer of low momentum

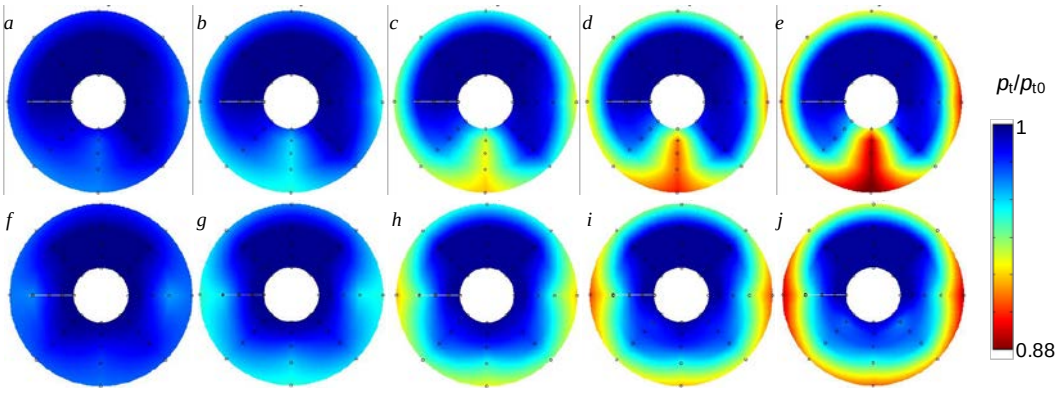

Figure 7. *Total pressure contour plots at the AIP for the baseline (a - e) and controlled flows by C_q = 0.01 (f), 0.009 (g), 0.0075 (h), 0.007 (i), and 0.0068 (j) at M = 0.36 (a,f), 0.45 (b,g), 0.58 (c,h), 0.64 (d,i), and 0.7 (e,j).*

fluid along the wall, which spans about ¾ of the AIP inner circumference. Such a redistribution clearly benefits the AIP distortion as large localized zone of low momentum fluid becomes diffused into a thin layer of reduced total pressure. Thereby, the distortion pattern becomes increasingly axisymmetric. Such a redistribution of the total pressure deficit is also consistent with the dynamics of the two large-scale vortices that are mirrored across the diffuser plane of symmetry, having a sense of rotation that carries the low-momentum fluid out of the central bottom wall, and along the wall upward. Again, such a global dynamics of the active flow control would be analogous to the active flow control effect in a BLI offset diffuser[24,25], just like in the baseline flows.

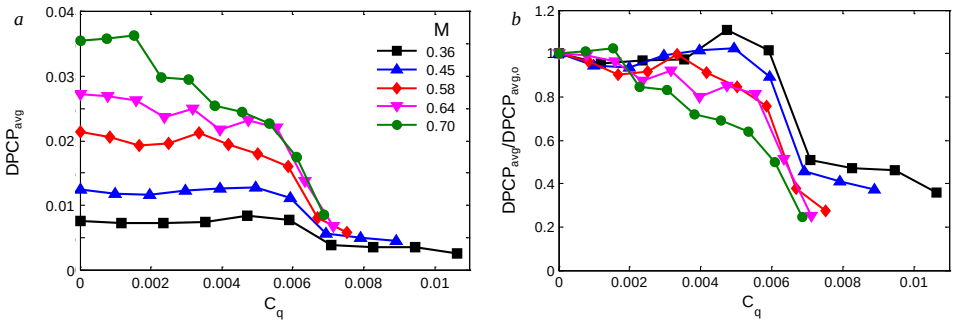

Figure 8. *Absolute (a) and relative (b) measure of the AIP total pressure distortion $DPCP_{avg}$ with the flow control mass flow rate coefficient C_q, at five diffuser Mach numbers M = 0.36 – 0.7.*

A summary of the flow control effect on the diffuser total pressure distortion, expressed by $DPCP_{avg}$, is shown in Figure 8a for all of the Mach number flows illustrated in Figure 7, and for a range of the flow control parameter C_q. As the distortion levels are very low for the two lowest Mach numbers, there is virtually no change at the lowest C_qs, which is followed by a sudden small drop and the leveling with further increase in C_q. As the diffuser Mach number is increased, there is a steady increase in $DPCP_{avg}$, on which the actuation at the lowest levels of C_q induce a moderate decrease in $DPCP_{avg}$, until C_q is increased past 0.5%, when any further increase in C_q up to about 0.7% results in a sharp reduction in $DPCP_{avg}$. The distortion levels are brought down to such a low level at $C_q \approx 0.7\%$ that any further increase in C_q does not result in any further improvement, i.e., the flow control effect is saturated. Therefore, the overall effectiveness of the applied flow control could be divided into three domains: (i) moderate reduction of the flow distortion for C_q = 0 – 0.5%, (ii) a sharp reduction in $DPCP_{avg}$ for C_q = 0.5 – 0.7% and (iii) saturation of the flow control effectiveness for C_q > 0.7%. Another interesting insight into the flow control effectiveness can be gained by consideration of the relative reduction in total pressure distortion under the flow control. Therefore, the absolute $DPCP_{avg}$ trends shown in Figure 8a are presented in Figure 8b as fractions of the average distortion of the corresponding base flow $DPCP_{avg,o}$. Besides a three-zone trend that can be also observed in Figure 8b (note that the final saturation level decreases with M, as the corresponding absolute levels are about the same in Figure 8a), it also indicates that the flow control effectiveness in a relative sense actually increases with M. Although this finding may appear counterintuitive, it is believed that the flow control simply acts on a higher distorted flow with increasing M, and is capable of making a stronger impact on it as compared to the flows with low levels of distortion where there is not much to be corrected by the flow control to begin with. In simpler terms, a flow control cannot be as effective under the flow conditions that do not create a source for the flow control utilization. It should be also added that above-stated increasing flow control effectiveness in a relative sense would eventually have an upper bound with continuing increase in M, which is clearly not reached in the present

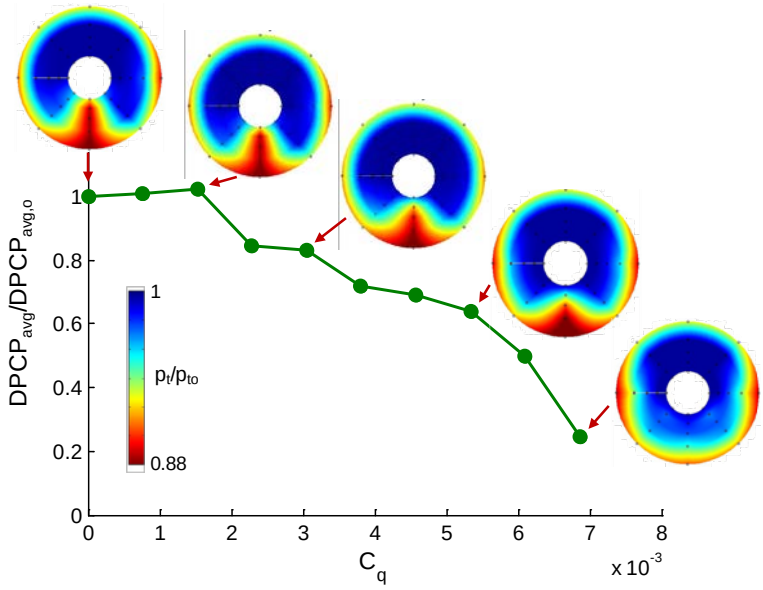

Figure 9. *AIP total pressure distortion parameter $DPCP_{avg}$ with the flow control mass flow rate coefficient C_q at M = 0.7, with characteristic contour plots of the AIP total pressure.*

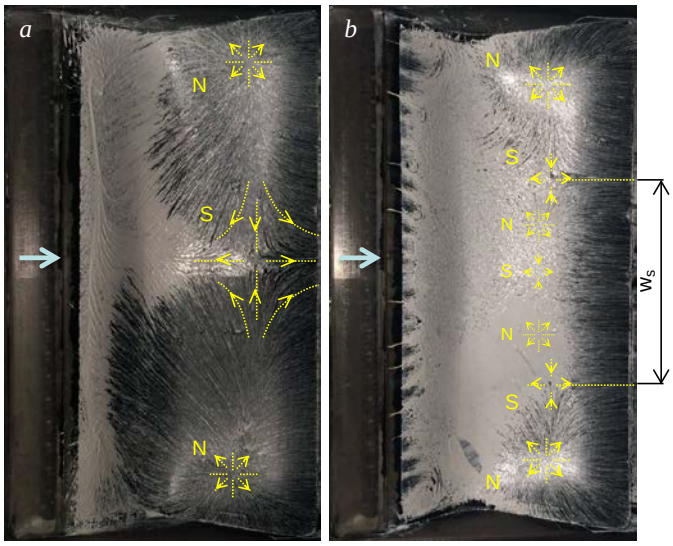

Figure 10. *Surface oil-flow visualization over the flow control insert for the baseline (a) and the controlled flow (b) at M = 0.58 at $C_q \approx$ 0.007. The flow is from left to right.*

test.

Figure 9 further illustrates relationship between the total pressure distortion patterns and the average distortion parameter $DPCP_{avg}$ for the highest Mach number flow, M = 0.7. As the flow control parameter C_q is increased from zero (no control), there is virtually no change in the average distortion, which is also see by almost unchanged distortion pattern relative to the base flow. As the distortion becomes affected by the flow control with further increase in C_q, it is seen that the peak total pressure deficit that was protruding up towards the duct axis begins to retreat, as it is pushed towards the wall and spread outward at $C_q \approx$ 0.3%. Such an alleviation of a previous sharp isolation of the low total pressure results in nearly 20% reduction in the average measure of distortion. Distortion parameter continues to decrease with C_q, and a notable sweep of the low momentum fluid up the diffuser wall is seen at the next characteristic AIP contour, at C_q just about 0.5%. As already stated in discussion of Figure 8, the highest flow response to the flow control is achieved 0.5% < C_q < 0.7%, as the $DPCP_{avg}$ sharply decreases, and the last AIP contour (C_q = 0.17%) shown in Figure 9 indicates the final total distortion pattern that amounts to notably reduced distortion parameter: the focused zone of low total pressure of the base flow is completely swept away and up the diffuser wall. As a side note, a somewhat larger layer of lower pressure up the wall, compared to that at the bottom, indicates that possibly even slightly better axisymmetric balance could be achieved at slightly lower C_q. It is conceivable that further increase in C_q past the optimal total pressure balance could have detrimental effect on distortion relative to the optimal control point.

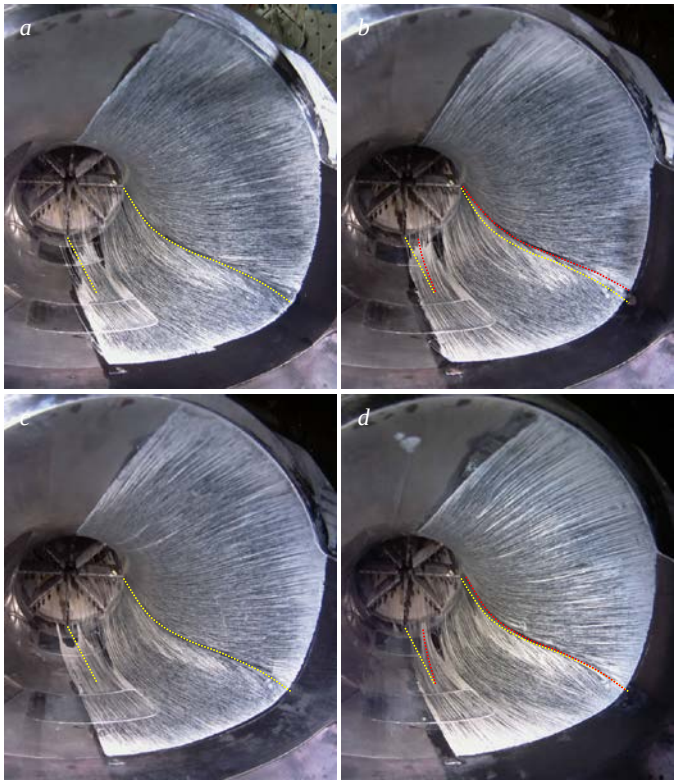

Figure 11. *Surface oil-flow visualization of the baseline (a, c) and the controlled flows (b, d, $C_q \approx$0.007) at M = 0.58 (a, b) and 0.7 (c, d). The AIP rake is seen at the downstream end.*

Surface oil-flow visualization is also utilized for elucidation of local and global flow topology within the diffuser and, in particular, downstream from the flow control jets. Oil for visualization is made out of a mixture of linseed oil and titanium-dioxide paint, where a balance between the two was determined iteratively, yielding a viscosity that matches the Mach number range and responds to the shear at the diffuser operating condition. First insight into the baseline and controlled flow topology is gained by utilizing surface oil-flow visualization over the flow control insert surface, where the oil is applied from just downstream from the jets array to the downstream end of the flow control insert. As an illustration of the flow control effect, two traces are shown in Figure 10 for the Mach number M = 0.58. Figure 10a indicates the baseline flow topology, which is dominated by the two reattachment domains separated by the central saddle point, and each having a node close to the side wall, as marked on the image. It

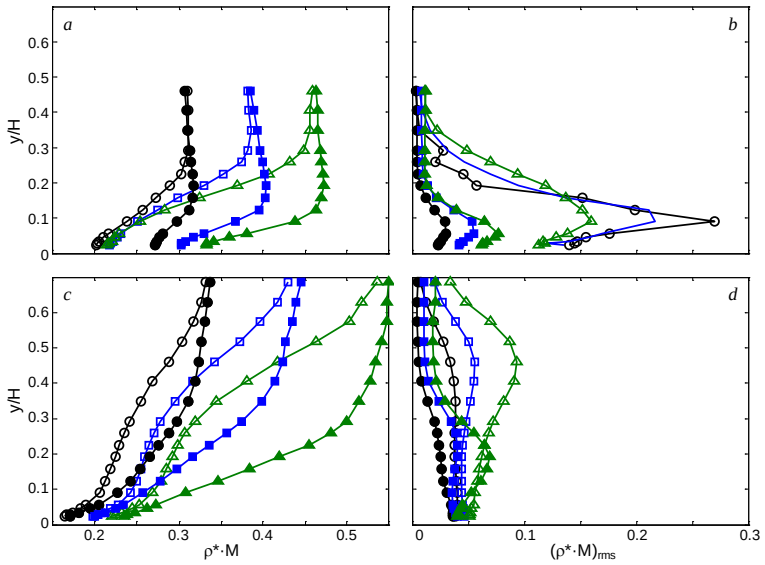

Figure 12. *Time-averaged $\rho \cdot U$ (a, c) and $(\rho \cdot U)_{rms}$ (b, d) profiles at the central upstream (a, b) and downstream (c, d) port for the baseline (open symbols) and controlled (solid symbols) flows at M = 0.36 (○), 0.45 (□), and 0.58 (Δ), and C_q = 0.7% (▲), 0.9% (■), and 1% (●).*

can be argued that the corner/end effects of the evolving D-shaped diffuser geometry induce the local corner flow reattachment at the nodes, which in turn forces the flow symmetry about the central plane through the saddle point. This reattachment dynamics also indicates highly three-dimensional flow in the separation bubble, and points to the flow directionality towards the central plane. The controlled (C_q = 0.7%) flow topology is shown in Figure 10b. As expected, there is a clear imprint of the flow control jets just downstream from the actuator array, and their effect is reflected further downstream in the reduction of the reattachment length of the separated flow. Besides changes in the global scales of the recirculating domain, its topology is also altered. The nodes from the local corner base flow reattachment are still present, but they are much more confined under the controlled flow. Each node has its own terminating saddle point in close proximity. Although it is not easily discernible from the central oil flow imprint due to the oil accumulation, there is at least another central combination of two nodes and a saddle, and possible even more such combinations exist between the two outer saddle points. Such a topology feature is believed to be related to the discrete nature of actuation, as the flow control jets are segmented. Regardless of the exact combination of the node and saddle points, the flow control generates a wide central portion of the reattaching flow (marked as w_s) with a quasi two-dimensional flow downstream from the flow reattachment, particularly about the central plane.

Besides the flow topology that is focused on the recirculating domain, global flow traces along the diffuser wall are visualized over representative surface area from downstream of the flow control insert to the AIP. An illustration of such visualization for both the base (uncontrolled) and the flows controlled by the total jet mass flow rate coefficient C_q = 0.7% are shown in Figure 11, for M = 0.58 and 0.7. There are two dominant features seen in the base flows (Figures 11a and c): a clear imprint of the streamwise vortex formed downstream from the recessed diffuser moldline over the flow control insert, and angularity of the flow approaching the central bottom section of the AIP where the largest deficit in total pressure is measured (cf. Figure 7a–e). Both of these features are emphasized by yellow marks overlaid atop of the corresponding images. Such an angularity of the flow approaching the AIP is possibly related to the angularity of the flow approaching the central plane seen in the upstream visualization in Figure 10a. The flow control has similar effect of both of these features at either Mach number (Figure 11b and d). First, the streamwise vortex trajectory becomes displaced outward from the central plane under the flow control (marked in red dots). Second, and even more importantly, the flow approaching the AIP becomes directed straight towards the AIP, instead under a notable angle (compare red and yellow marked traces), which ultimately results in significant suppression of total pressure distortion in this area (cf. Figure 7f–j). Just as in the base flow, the altered flow directionality in the approach to AIP can be tied to the flow "straightening" about the central plane in the upstream flow visualization seen in Figure 10b.

Besides the local and global flow topology, it is critical to capture the diffuser flow dynamics in either uncontrolled or controlled flows, which requires time-resolved flow measurements. As stated in Section II, both hot-wire anemometry and PIV are utilized for that purpose. Hot-wire characterization of the flow control effects is presented in Figure 12, where the controlled and uncontrolled $\rho \cdot U$ and $(\rho \cdot U)_{rms}$ profiles are shown for three diffuser Mach numbers, and both the 'reattachment' and AIP measurement stations (cf. Figure 3b). It is interesting to note that downstream from the recirculating bubble (Figure 12a) the reattached flow induces velocity deficit only up to about $y/H \approx 0.33$ away from the wall, even in the uncontrolled flows. Contrary to the station, as the flow decelerates along diffuser, the portion of the flow that experiences deficit grows, and, the bulk (unaffected) flow does not become reached even at distances close to $y/H \approx 0.66$ (Figure 12c). Upon the flow control activation, velocity deficit at

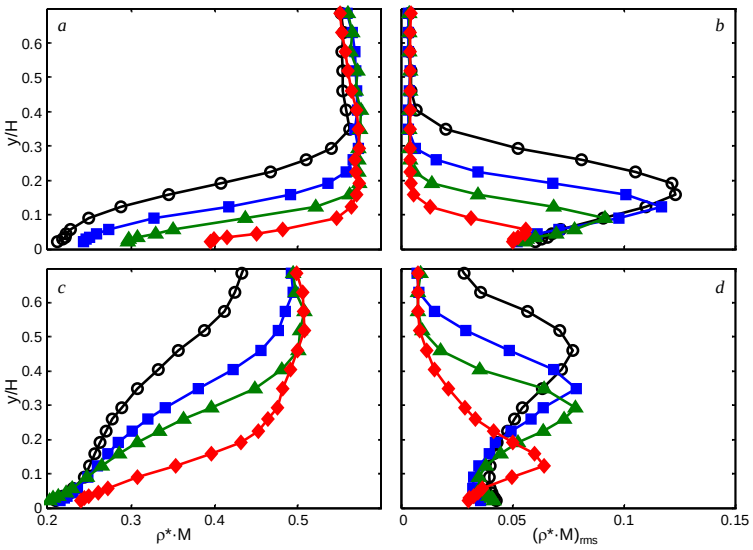

Figure 13. *Time-averaged $\rho \cdot U$ (a, c) and $(\rho \cdot U)_{rms}$ (b, d) profiles at the central upstream (a, b) and downstream (c, d) port for the baseline (○, M_{AIP} = 0.67) and controlled flows at C_q = 0.2% (■), 0.5% (▲), and 0.7% (♦).*

either station becomes significantly reduced, and the affected flow is pushed towards the wall. It is noteworthy that the flow control effectiveness appears to be more pronounced at higher diffuser Mach numbers, as the increase in velocity becomes proportional to the diffuser Mach number. This result may be attributed to the fact that the control jets utilize the flow momentum when vectoring the diffuser flow and suppressing the separation bubble. Therefore, as long as they are capable of vectoring the flow of increasing momentum (as the diffuser M is increased), they should impose a stronger impact on the downstream flow. The upstream $(\rho \cdot U)_{\text{rms}}$ profiles (Figure 12b) point to strong flow fluctuations in the baseline flow, as this location is not far removed from the flow reattachment zone. It is also interesting to note that the peak levels of fluctuation appear to decrease with increase in M, which may be related to the faster downstream dissipation of the smaller-scale fluctuations at higher Mach numbers. Contrary to the baseline flow, as the flow control is applied, a rather dramatic suppression in the fluctuation levels is observed, with the highest suppression at lowest diffuser Mach number, in excess of 80%. At the downstream location (Figure 12d), high levels of fluctuations close to the wall have already died out, and the peak fluctuations levels are associated with the highest shear of the velocity profiles, where the peak amplitudes are several-fold lower than at the upstream station (Figure 12b), and, contrary to the upstream station, increase with M. Nonetheless, the effect of the flow control on the $(\rho \cdot U)_{\text{rms}}$ is similar at the downstream station, as the levels of fluctuations generally decrease with the flow control, and the peak levels become pushed towards the wall in all of the cases.

The effect of the varying flow control parameter, mass flow rate coefficient C_q, is shown in Figure 13 for the diffuser mach number M = 0.67. Both the $\rho \cdot U$ and $(\rho \cdot U)_{\text{rms}}$ profiles are shown for the base and the flows controlled by C_q = 0.2, 0.5, and 0.7% at both the reattachment zone and upstream from the AIP. It is interesting to note that

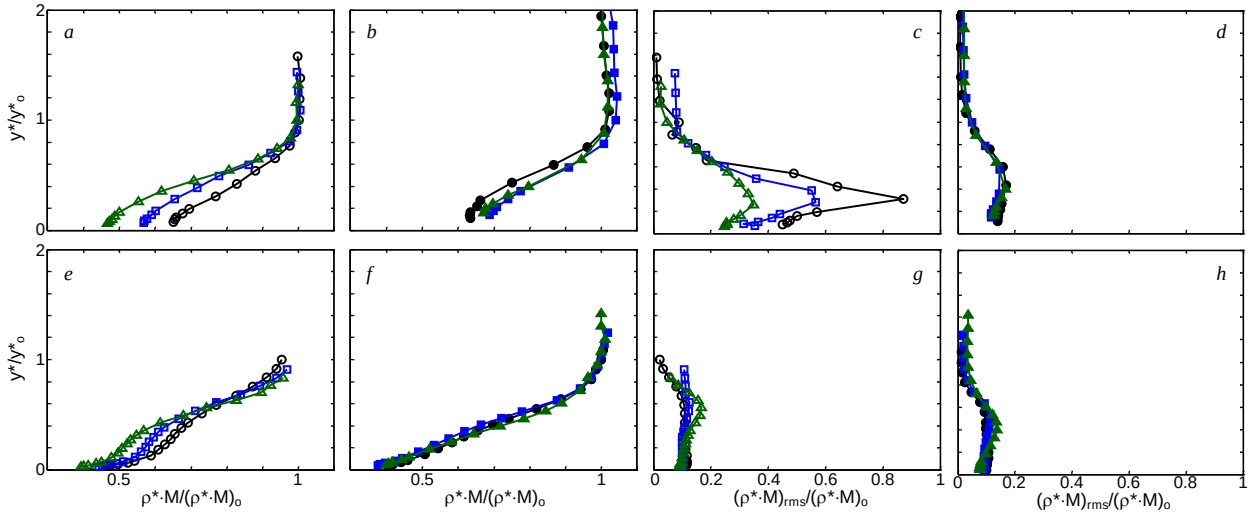

Figure 14. *Time-averaged $\rho \cdot U$ (a, b, e, f) and $(\rho \cdot U)_{rms}$ (c, d, g, h) profiles at the central upstream (a–d) and downstream (e–h) port for the baseline (open symbols) and controlled flows (solid symbols) at C_q = 0.6% and Mach numbers M = 0.36 (black), 0.45 (blue), and 0.58 (green).*

even at the lowest actuation level, a notable favorable effect is measured both in terms of the mean $\rho \cdot U$ profiles and $(\rho \cdot U)_{rms}$ fluctuations. The measurements downstream from the flow reattachment (Figure 13a) show rather proportional decrease of $\rho \cdot U$ deficit as C_q is increased, while the $(\rho \cdot U)_{rms}$ profiles (Figure 13b) proportionally show a peak fluctuation amplitude decrease, having a simultaneous gradual displacement towards the wall. At the measurement station upstream from the AIP, the mean $\rho \cdot U$ profiles (Figure 13c) particularly emphasize effectiveness of the highest C_q, having the bulk flow reached at about y/H = 0.56 away from the surface. The $(\rho \cdot U)_{rms}$ profiles (Figure 13d) indicate a strong effect on the peak $(\rho \cdot U)_{rms}$ displacement towards the wall with an increase in C_q and a rather mild effect on the suppression of the peak levels.

To test how diffuser flow responds to the same relative actuation level, diffuser flows at different Mach numbers are controlled by the fixed jet mass flow rate coefficient C_q. Figure 14 shows $\rho \cdot U$ and its $(\rho \cdot U)_{rms}$ fluctuation profiles for the three diffuser flow rates that correspond to the AIP M = 0.36, 0.45, and 0.58, at both the downstream from reattachment (Figures 14a-d) and upstream from AIP (Figures 14e-h), where all the profiles are scaled by their invariant magnitudes far from the wall, and length scales by their distance from the wall. Upstream baseline mean profiles (Figure 14a) indicate characteristic velocity deficit past the reattaching flow, where the deficit increases with the diffuser flow rate. As the flow becomes decelerated in the downstream direction, averaged profiles develop inflection point, as seen in Figure 14e. When the flow control is applied, it is shown that the mean profiles become self-similar at either measurement station (Figures 14b and f). Such an outcome indicates that C_q is a characteristic flow control parameter that can be used for either predictive purposes of the flow evolution within the controlled diffuser flow, or, alternatively, for estimating the flow control requirements under any other diffuser flow rate within the tested bounds. Besides a clear indication about the mean profiles self-similarity, the controlled profiles also indicate the altered nature of the flow: both upstream and downstream profiles indicate similar behavior where the velocity deficit is significantly reduced at the upstream measurement station, and subsequently grows under the adverse pressure gradient (Figure 14f). A measure of fluctuations $(\rho \cdot U)_{rms}$ that correspond to the baseline flows are shown in Figures 14c and g. Immediately downstream from the flow reattachment (Figure 14c), the $(\rho \cdot U)_{rms}$ levels are significantly increased, having peaks at the elevations that correspond to the highest shear in the $\rho \cdot U$ profiles. Also, the peak levels decrease with increased diffuser flow rate. However, as the flow evolves in the downstream direction, the highest flow rates develop higher peak fluctuation amplitudes and the order becomes inverted (compare Figure 14g to c). At the same time, overall $(\rho \cdot U)_{rms}$ levels are several-fold lower than at the upstream station. Once the flow control is applied, the region of high $(\rho \cdot U)_{rms}$ fluctuations becomes significantly suppressed at the upstream station, while the levels and distributions at the downstream station do not differ much from already low levels of the uncontrolled flows.

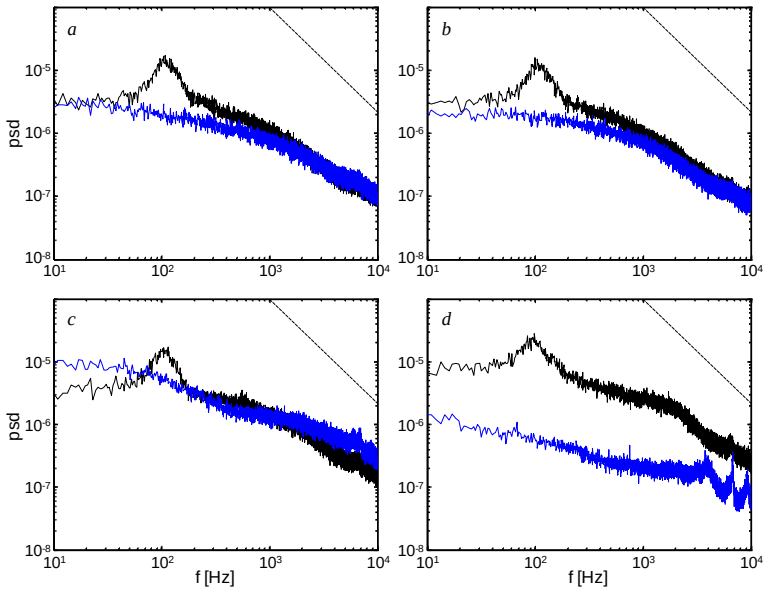

Figure 15. *Baseline (—, C_q = 0) and controlled (—, C_q = 0.6) power spectra of $\rho \cdot U$ fluctuations at downstream central measurement stations (M= 0.58) at y/H = 0.022 (a), 0.056 (b), 0.19 (c), and 0.35 (d) away from the wall.*

Additional insight into the flow control effect on the diffuser flow can be gained by analysis of the spectral content of the $\rho \cdot U$ fluctuations. Figure 15 shows power spectra of the $\rho \cdot U$ fluctuations at four characteristic distances away from the wall, which correspond to the base and controlled flow for the highest Mach number profiles at the AIP measurement station shown in Figure 12c and d. The most notable feature of the base flow spectra is the emergence of a broad spectral feature close to f = 100 Hz, which could be attributed to the trapped vorticity unsteadiness and possible feedback from the reattachment zone. A common spectral feature of the controlled flow at each measured elevation is that this dominant frequency becomes fully suppressed. Therefore, it can be argued that the flow control does not only change separation global scales, as seen in the flow visualization (cf. Figures 10 and 11),

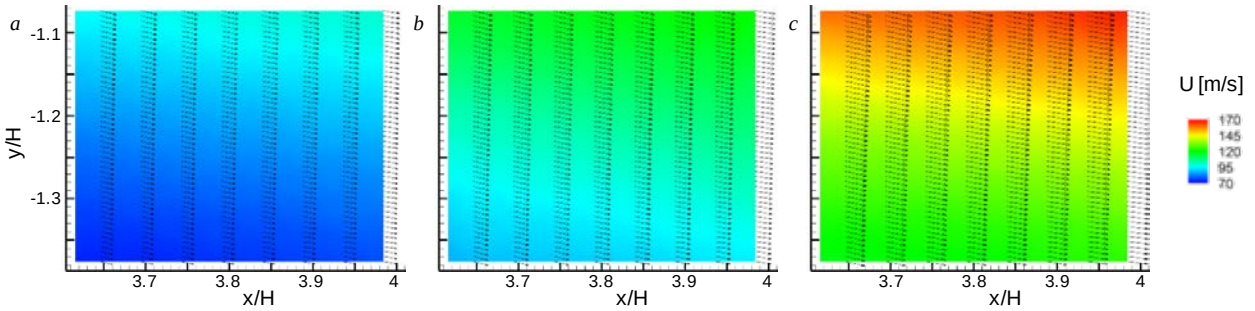

Figure 16. *Contour plots of the streamwise velocity component with equidistant velocity profiles for the baseline (uncontrolled) flows at M = 0.36 (a), 0.45 (b), and 0.67 (c).*

but also affects its dynamics, and suppresses its dominant unsteadiness. The other spectral features of the controlled flow relative to the baseline appear to be elevation dependent, which is partially attributed to the fixed spatial measurement points, while the flow becomes significantly changed (cf. Figure 12c). Two spectra closest to the wall (Figure 15a and b) clearly indicate a broadband suppression of fluctuations, asymptotically approaching the base flow levels at the highest frequencies. An interesting switch is measured at y/H = 0.19, where the controlled flow exhibit elevated levels of fluctuating energy at both ends of the spectra, while still suppressing the baseline dominant frequency. This is not surprising, given that this elevation coincides with the peak $(\rho U)_{rms}$ levels in the controlled flow, as seen in Figure 12d. This is the only localized domain where the controlled flow fluctuation levels exceed those of the baseline flow. Finally, as the last measurement point (y/H = 0.35) approaches the bulk flow in the controlled case, there is a rather dramatic drop in the fluctuation levels (Figure 15d) relative to the base flow.

While the hot-wire measurements provide moderate spatial and high temporal resolution of the flow 'line segments' downstream from reattachment and upstream from the AIP, PIV measurements about the same access locations are aimed at detailed resolution of the flow close to the wall. Prior to boundary layer characterization, an initial set of PIV measurements is focused on the larger region of the flow away from the wall that is positioned about 0.5H upstream from the AIP, and measures 40 × 20 mm (see Figure 3b). Figure 16 shows the contour plots of the averaged streamwise velocity component for the base flows, with the overlaid equidistant velocity profiles for three diffuser flow rates (M = 0.36, 0.45, and 0.67). This field of view covers a portion of the flow between the bulk duct flow and a near-wall region. Hence, velocity profiles do not reach peak diffuser velocities at the outer end, but they do capture velocity decrease towards the wall, without approaching the boundary layer. These velocity contours also indicate diffuser angle, as the velocity contour follow geometry angularity in the downstream x-direction. Flow control effectiveness is illustrated in Figure 17, where the diffuser flow that corresponds to M = 0.67 (Figure 16c) is controlled by the fluidic-jet actuation at C_q = 0.7%. Figure 17a shows the controlled flow field equivalent to the baseline flow shown in Figure 16c. Velocity deficit seen in the baseline flow is altered within the full field of view, as the high-momentum fluid is brought towards the wall under the flow control. Consequently, extent of the flow with lower momentum is compressed closer to the wall (outside of the field of view), which is attributed to the upstream suppression of the trapped vorticity region, immediately downstream from the flow separation. Further insight into the velocity/momentum increase across the measurement domain is gained by subtracting the baseline flow field from the controlled one. The resulting flow difference is plotted in Figure 17b. It is noted that the momentum increase is directed towards the wall, i.e., the velocity gain is smallest at the bulk flow side and increases towards the wall, exceeding ΔU = 40 m/s along the side closest to the wall.

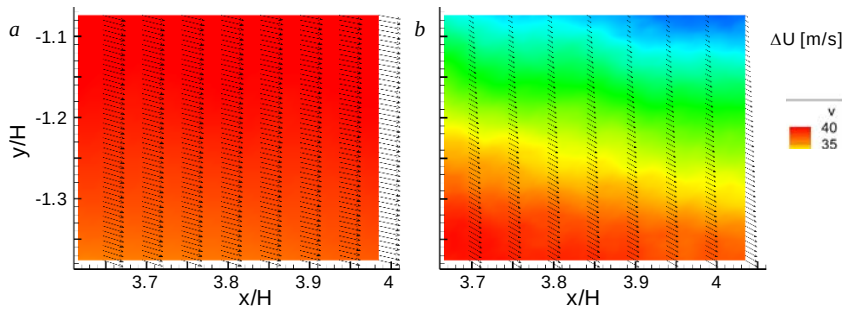

Figure 17. *Contour plots of the streamwise velocity component with equidistant velocity profiles for the flow at M = 0.67 controlled at C_q = 0.7% (a, contour map the same as in Fig. 17) and the corresponding velocity field difference ΔU between the controlled and uncontrolled flow (b).*

In order to resolve the wall flow region with finer resolution, PIV field of view is further refined at both measurement stations, as

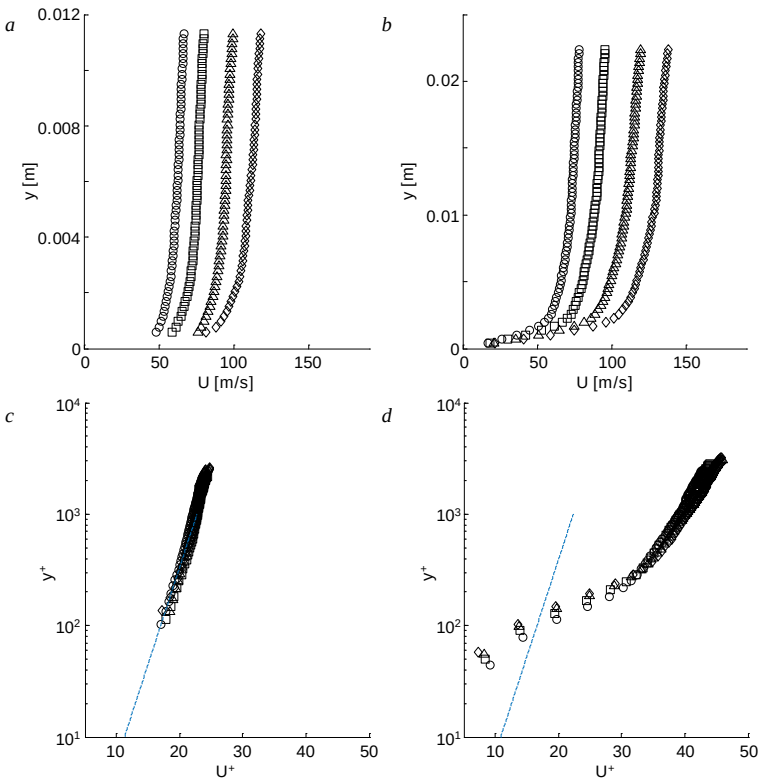

Figure 18. *Time-averaged base flow streamwise velocity profiles downstream from the flow reattachment (a,c) and upstream from the AIP (b,d) in dimensional (a,b) and wall (c,d) coordinates for M = 0.36 (○), 0.45 (□), 0.58 (Δ), and 0.7 (◊). Logarithmic law $U^+ = 2.5 \cdot \ln y^+ + 5.5$ (---) is shown for reference.*

schematically shown in Figure 3b. As the individual PIV measurement domain becomes reduced in size, it is needed to take a multi-window measurement to capture velocity profiles with both the fine resolution and sufficient extent. Hence, these measurements utilize two partially-overlapping measurement windows to enable a composite flow field representation. Baseline flows are first characterized in the absence of the flow control, and four characteristic near-wall flow fields are measured both downstream from the reattachment and upstream from the AIP, for the Mach numbers M = 0.36, 0.45, 0.58, and 0.7. Boundary layer profiles are extracted from each of the ensemble-averaged flow fields, and are shown in Figure 18 for all of the baseline flows. First, it should be noted that, in spite of the great care of surface reflections under laser illumination, there is narrow strip of flow right at the wall that cannot be resolved by PIV measurements, and it is estimated that the closest measured velocity is about 0.6 mm away from the wall at the upstream, and about 0.4 mm at the downstream measurement location. As the upstream location is close to the flow reattachment zone, the regrowing boundary layer is rather thin, as it can be seen in the profiles in Figure 18a. Another feature that is seen in the velocity profiles is that there is significant velocity deficit in all of the profiles, relative to the diffuser Mach number, as the flow just reattached and begins to accelerate close to the wall. Given the adverse pressure gradient of the diffuser, it is expected that the boundary layer closer to the AIP would be thicker, which is clearly seen in Figure 18b, but the profile shapes also seem altered from a canonical turbulent boundary layer profiles, ostensibly due to the three-dimensional motions that are known to take the high-momentum flow away from the surface in this region. To further test how the measured mean velocity profiles of the base flows compare to canonical turbulent boundary layer profiles, the measured profiles are reduced to wall coordinates: $U^+ = \overline{U}/u_\tau$ and $y^+ = yu_\tau/\nu$. In order to form these coordinates, additional measurements of the flow static pressure and temperature at the wall are made for all of the flow conditions, and the fluid properties are extracted. However, the biggest uncertainty is these estimates is in the mean velocity gradient at the wall, which cannot be directly measured. Its initial value is calculated based on the first measurement point of the mean velocity profile, and it is corrected by a multiplication factor based on the numerically-resolved full boundary layer profiles. The scaled boundary layer profiles that correspond to Figures 18a and b are shown in Figure 18c and d, respectively. In addition, a canonical turbulent boundary layer log-law profile $U^+ = 2.5\ln y^+ + 5.5$ is plotted for reference. It is seen that the upstream boundary layer profiles (Figure 18c) closely follow canonical log-low profile, in spite that the bulk flow is not fully developed, as the boundary layer grows past the flow reattachment. Contrary to this boundary layer evolution, the profiles upstream from the AIP (Figure 18d) significantly depart from the canonical turbulent boundary layer profile, as the secondary flow significantly impacts the central wall flow and reduce its momentum (which results in reduction in the total pressure). As the flow momentum is reduced close to the wall, the wall shear stress is lowered, which in turn results in increase U^+ for a given outer flow speeds, which is seen in the profiles shown in Figure 18d.

The flow control effect on the boundary layer mean velocity profiles is illustrated in Figure 19 for all of the base flows depicted in Figure 18, and for the three jet mass flow rate coefficients C_q. It should be pointed out that the three C_qs for each diffuser flow were fixed at the total mass flow rate though the jets, such that C_q magnitude

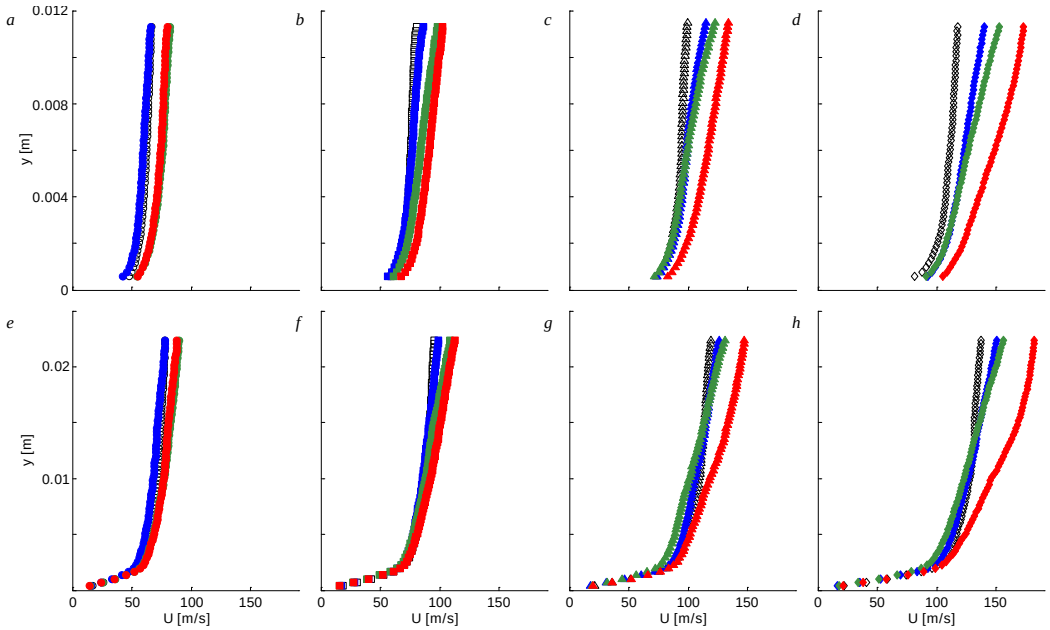

Figure 19. *Time-averaged near-wall streamwise velocity profiles for the base (open symbols) and controlled flows downstream from the flow reattachment (a–d) and upstream from the AIP (f–h) at M = 0.36 (a,e), 0.45 (b,f), 0.58 (c,g), and 0.7 (d,h). $C_q \times 10^3$ varies between: 4 – 11 (a,e), 3 – 9 (b,f), 3 – 8 (c,g), and 2 – 7 (d,h), where increasing C_q is colored from blue to green to red.*

actually decreases with an increase in M. It is seen, as expected, that velocity increases, in principle, with C_q regardless of the measurement domain, while the highest effect is clearly seen at the highest level of C_q. One difference between the upstream and downstream profiles appears immediately next to the wall. While the controlled velocity profiles downstream from the reattachment (Figures 19a–d) clearly indicate increase in flow velocity in the closest proximity to the wall, profiles upstream from the AIP (Figures 19f–h) are predominantly affected away from the wall, and a change close to the wall is negligible. Also, the flow control at the lower Mach number flows does not seem to alter much the shape of the velocity profiles (e.g., Figures 19a–b and e–f), contrary to the flows at higher Mach numbers (Figures 19c–d and g–h). Another interesting feature of the controlled flows is that appears the flow control effectiveness increases with the diffuser Mach number, in spite the fact that the flow control C_q decreases at the same time (as the jets total flow rate is kept constant). The same trend was observed during analysis of the average total pressure distortion parameter with variation of both M and C_q (cf. Figure 8). Although this outcome might seem counterintuitive, it can be argued that the flow control takes advantage of the diffuser flow momentum and its turning due to the reattachment over the local separation, and that "utilized" flow momentum increases with M and results in the increased flow control effect.

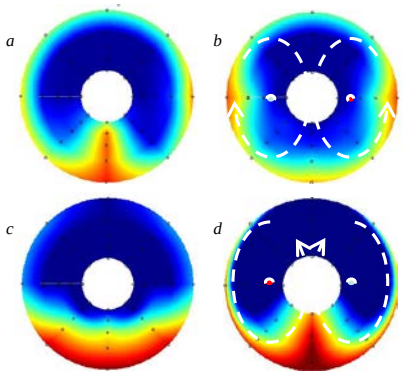

Figure 20. *Illustration of the equivalent flow control effect on the AIP total pressure distortion (a,b) and the secondary flow redistribution of the total pressure distortion for the think inlet boundary layer (c-d, Gissen et al.[24]).*

As already noted in discussion related to Figure 7, several parallels can be drawn between the current work on thin diffuser boundary layer flows with separation and thick diffuser boundary layer flows without separation[24]. This analogy is revisited in Figure 20, where equivalent effect of the applied flow control in the current work is represented in the upper row. It is shown that the base (uncontrolled) flow distortion (Figure 20a) measured at the AIP becomes redistributed along the diffuser wall under the action of the flow control (Figure 20b), which is equivalent to the action of the two large-scale counter-rotating vortices. Similar effect of the base flow secondary vortices was observed in the thick boundary layer-ingesting diffuser flow[24], which is illustrated in the lower row. The thick boundary layer brings significant momentum/total pressure deficit into the diffuser, which is illustrated in Figure 20c. However, total pressure distortion that is measured at the AIP has a similar

structure to that measured in the present investigation. It is known that two large scale counter-rotating vortices that evolve within the diffuser are responsible for redistribution of the incoming flow distortion (Figure 20c) to the AIP total pressure distortion (Figure 20d). The flow control effect in both the present and the past studies[24,25] in offset diffuser flow appears to counteract the effect of the naturally-evolving secondary flows, regardless of whether a source of low momentum fluid is entrained thick boundary layer or local separation. Such similarities between both base and controlled flows open a possibility that the flow control approach developed for the diffuser thin boundary layer flow with separation could be utilized for diffuser flow that ingest thick boundary layer, and vice versa.

V. Conclusions

The performance of compact, aggressive diffusers in advanced supersonic propulsion systems is limited by internally-confined flow separation coupled with secondary flow that give rise to severe flow distortions at the engine inlet. Because vorticity concentration, trapped within the confined separated flow domain, is susceptible to flow actuation, it provides significant leverage for modification of the secondary flow and mitigation of flow distortions. The present investigations focus on a demonstration of the effectiveness of hybrid flow control approach that is based on the coupling between a concentration of trapped vorticity engendered by deliberate modification of the internal surface of an offset diffuser and a spanwise array of surface-integrated fluidic-oscillating jets for modifying the evolution of the secondary flow. The actuation is utilized to control the strength and scale of the trapped vorticity within the confined separation bubble and its effect on the secondary flow is measured by the ensuing reduction in the total pressure distortion at the diffuser outlet. The local and global characteristics of the diffuser flow in the absence and presence of the actuation are investigated at Mach numbers up to $M = 0.7$, in a D-shape to circular diffuser ($D = 12.7$ cm) that is offset by one diameter over $L/D \approx 3$. The trapped vorticity is formed within a moldline recess of the internal diffuser surface having characteristic streamwise scale of 0.7D, and the spanwise array of fluidic-oscillating jets (operating between 7 and 9 kHz), is placed just upstream of the recess and actuation is effected at jet mass flow rate ratio C_q of up to 1%. Flow diagnostics included a standard forty-probe AIP total pressure rake, surface oil-flow visualization, hot-wire anemometry, and particle image velocimetry.

The suppression effectiveness of the total pressure distortion, as measured by the average distortion parameter $DPCP_{avg}$ at the interface plane between the diffuser and an engine (AIP) over a range of Mach numbers, exhibits three characteristic domains namely, initial moderate suppression within the range $0 < C_q < 0.5\%$, followed by a sharp reduction for $0.5 < C_q < 0.7\%$, and finally saturation of the flow control effectiveness for $C_q > 0.7\%$ as the diminished distortion level remains nearly invariant. The present measurements show that the relative increase in the effectiveness of the fluidic actuation increases with M reaching about 80% reduction in distortion at $M = 0.7$ and $C_q = 0.7\%$.

Surface oil visualization and cross stream velocity measurements indicate that the evolution secondary streamwise vortical structures within the diffuser gives rise to the distortion measured at the AIP. The base flow exhibits the effects of a large scale counter-rotating vortex pair that each advects low-momentum fluid along the bottom surface of the diffuser symmetrically towards the center plane leading to significant distortion in the presence of the trapped vortex within the closed separation domain in the upstream surface recess. In the presence of actuation, the interaction of the actuation jets with the trapped vortex leads to considerable weakening of the strength of these vortices. This effect may be thought of as giving rise to an induced pair of counter-rotating vortices of opposite sense that leads to recession of the low momentum fluid and its symmetric redistribution along the inner surfaces at the AIP. This, in turn, significantly reduces the overall flow distortion by confining it to a thin wall layer and increasing its symmetry about the diffuser's centerline. Spectral analysis of the velocity fluctuations in the attached flow downstream of the trapped vortex in the presence the flow control point not only to broadband suppression in the energy of the unsteady flow but also to full suppression of a dominant low-frequency spectral peak in the base flow. These findings indicate that the utility of hybrid control with a deliberate trapped vortex may be effective in suppressing the adverse effects of "natural" separation domains on flow distortion within aggressive diffusers. Furthermore, the effectiveness of present hybrid approach also indicates that it could be useful for suppression of similar AIP flow distortions that are effected by secondary flow structures which are induced even in the absence of internal separation when the boundary layer of the incoming flow at the diffuser's inlet is relatively thick (e.g., for a thick boundary layer ingestion in blended-wing body configurations).

Acknowledgment

This work has been supported by ONR, monitored by Drs. Joseph Doychak and Knox Millsaps.

References

[1]Vakili, A., Wu, J. M.., Liver, P., Bhat, M. K., "Flow Control in a Diffusing S-Duct," *AIAA Paper* AIAA-85-0524, 1985.

[2]Reichert, B. A. Wendt, B. J. "Improving Curved Subsonic Diffuser Performance with Vortex Generators." *AIAA Journal*, Vol. 34, No 1, 1996.

[3]Owens, L.R., Allan, B.G., Gorton, S.A., "Boundary-Layer-Ingesting Inlet Flow Control," *Journal of Aircraft*, Vol. 45, No. 4, 2008.

[4]Jirásek, A., "Development and Application of Design Strategy for Design of Vortex Generator Flow Control in Inlets," *AIAA paper* AIAA-06-1050, 2006.

[5]Anderson, B.H., Gibb, J. "Study on Vortex Generator Flow Control for the Management of Inlet Distortion," *Journal of Propulsion and Power*, Vol. 9 No. 3, 1993.

[6]Anabtawi, A.J., Blackwelder, R.F., Lissaman, B.S.P, Liebeck, R.H., "An Experimental Investigation of Boundary Layer ingestion in a Diffusing S-Duct With and Without Passive Flow Control," *AIAA Paper* AIAA-99-0739, 1999.

[7]Anderson, B.H., Baust, D.H., Agrell, J. "Management of Total Pressure Recovery, Distortion and High Cycle Fatigue in Compact Air Vehicle Inlets," *NASA/TM*. 2002-212000, 2002.

[8]Anderson, B.H., Miller, D.N., Addington, G.A., Agrell, J. "Optimal Micro-Vane Flow Control for Compact Air Vehicle Inlets," *NASA/TM*. 2004-212936, 2004.

[9]Tournier, S., Paduano, J.D."Flow Analysis and control in a Subsonic Inlet," *AIAA Paper AIAA*-05-4734, 2005.

[10]Anderson, B., Tinapple, J., and Surber, L. "Optimal Control of Shock Wave Turbulent Boundary Layer Interactions Using Micro-Array Actuation," *AIAA Paper AIAA*-2006-3197, 2006.

[11]Babinsky, H. Li, Y., Pitt., Ford, C.W. "Optimal Microramp Control of Supersonic Oblique Shock-Wave/Boundary-Layer Interactions," *AIAA Journal*, Vol. 47, 668-675, 2009.

[12]Weigl, H. J., Paduano, J. D., Frechette, L. G., Epstein, A. H., Greitzer, E. M., Bright, M. M., & Strazisar, A. J. "Active stabilization of rotating stall and surge in a transonic single stage axial compressor." Proceedings of *ASME 1997 International Gas Turbine and Aeroengine Congress and Exhibition*, Paper 97-GT-411, 1997.

[13]Scribben, A.R., Ng, W., Burdiso, R., "Effectiveness of a Serpentine Inlet Duct Flow Control Technique at Design and Off-Design Simulated Flight Conditions" *J. Turbomachinery*, Vol. 128, No. 2, pp. 332-339, 2006.

[14]Anderson, B.H., Miller, D.N., Addington, G.A., Agrell, J. "Optimal Micro-Jet Flow Control for Compact Air Vehicle Inlets," *NASA/TM*. 2004-212937.

[15]Vaccaro, John. Vasile, J. Amitay, M. "Active Control of Inlet Ducts." *AIAA Paper* AIAA-2008-6402., 2008.

[16]Rabe, Angela C. "Effectiveness of a Serpentine Inlet Duct Flow Control Scheme at Design and Off-Design Simulated Flight Conditions" *PhD Thesis Virginia Tech*. 2003.

[17]Amitay, M., Pitt, D., Glezer, A. "Separation Control in Duct Flows," *J. Aircraft*., Vol. 39, No. 4, 2002, pp. 616-620.

[18]Gissen, A. N., Vukasinovic, B., and Glezer, A. "Controlled Streamwise Vorticity in Diffuser Boundary Layer using Hybrid Synthetic Jet Actuation" *AIAA Paper*, AIAA-2009-4021, 2009.

[19]Anderson, B.H., Mace, J.L., Mani, M.,"Active "Fail Safe" Micro-Array Flow Control For Advanced Embedded Propulsion Systems," *AIAA Paper* AIAA-09-741, 2009.

[20]Godard, G. Stanislas, M. "Control of a decelerating boundary layer. Part 1: Optimization of passive vortex generators." *Aerospace Science and Technology*, Vol. 10, pp. 181-191. 2006.

[21]Dagget, David L. Kawai, R. Friedman, D. "Blended Wing Body Systems Studies: Boundary Layer Ingestion Inlets with Active Flow Control" *NASA/CR*. 2003-212670.

[22]Delot, A. L., Garnier, E., and Pagan, D. "Flow control in a high-offset subsonic air intake." *AIAA Paper*, AIAA-2011-5569, 2011.

[23]Harrison, N. A., Anderson, J., Fleming, J. L., and Ng, W. F. "Active flow control of a boundary layer-ingesting serpentine inlet diffuser." *Journal of Aircraft*, Vol 50, no. 1, 262-271, 2013

[24]Gissen, A. N., Vukasinovic, B., McMillan, M. L., and Glezer, A., "Distortion Management in a Boundary Layer Ingestion Inlet Diffuser Using Hybrid Flow Control", *J. Propul. Power*, Vol 30, pp. 834-844, 2014.

[25]Gissen, A. N., Vukasinovic,B., and Glezer, A. "Dynamics of flow control in an emulated boundary layer-ingesting offset diffuser" *Exp. Fluids*, Vol 50, 1794, 2014.

[26]Gartner, Jeremy, and Amitay, M. "Effect of boundary layer thickness on secondary structures in a short inlet curved duct." *International Journal of Heat and Fluid Flow*, Vol. 50, pp. 467-478, 2014.

[27]Gartner, Jeremy, and Amitay, M. "Flow Control in a Diffuser at Transonic Conditions." *AIAA Paper*, AIAA-2015-2484, 2015.

[28]*Society of Automotive Engineers* Aerospace Recommended Practice 1420 Revision B, 2002-03-01